Monitoring polariton dynamics in the LHCII photosynthetic antenna in a microcavity by two-photon coincidence counting

Zhedong Zhang, Prasoon Saurabh, Konstantin E. Dorfman, Arunangshu Debnath, and Shaul Mukamel

Citation: The Journal of Chemical Physics **148**, 074302 (2018);
View online: https://doi.org/10.1063/1.5004432
View Table of Contents: http://aip.scitation.org/toc/jcp/148/7
Published by the American Institute of Physics

Monitoring polariton dynamics in the LHCII photosynthetic antenna in a microcavity by two-photon coincidence counting

Zhedong Zhang,[1,a)] Prasoon Saurabh,[1] Konstantin E. Dorfman,[1,2,b)] Arunangshu Debnath,[1,c)] and Shaul Mukamel[1,d)]
[1]*Department of Chemistry, University of California Irvine, Irvine, California 92697, USA*
[2]*State Key Laboratory of Precision Spectroscopy, East China Normal University, Shanghai 200062, China*

(Received 12 September 2017; accepted 23 January 2018; published online 15 February 2018)

The relaxation dynamics of light-harvesting complex II in an optical cavity is explored theoretically by multidimensional photon coincidence counting spectroscopy. This technique reveals the dynamics in both single (e) and double (f) excitation bands. We study how the polariton dynamics are affected by coupling to photon modes and molecular vibrations described by a realistic spectral density at 77 K. Without the cavity, the e- and f-band energy transfer pathways are not clearly resolved due to the line broadening caused by fast exciton dephasing. The strong coupling to cavity photons results in well-resolved polariton modes. The hybrid nature of polaritons slows down their energy transfer rates. *Published by AIP Publishing.* https://doi.org/10.1063/1.5004432

I. INTRODUCTION

The hybrid dressed photon-matter states, known as polaritons, are joint molecule/photon states, involving coherence between excitons and photons, induced by the strong molecule-photon interaction in microcavities.[1–6] The hybrid nature of polaritons could affect the dynamical pathways[7–10] as well as chemical reaction processes.[11–15] In this article, we focus on exciton dynamics in the double excitation manifold. This has been previously investigated in free complexes (no cavity) by third-order nonlinear spectroscopy.[16,17] Coupling J-aggregates to cavity modes provides an artificial ultrafast energy-transfer pathway of excitons, which can be detected by fluorescence.[18] The strong coupling of vibrational transitions to cavity modes modifies the relaxation dynamics and energy exchange. This was recently demonstrated by pump-probe infrared spectroscopy of the cavity-coupled C–O stretching mode of $W(CO)_6$.[19] The single-exciton relaxation pathways may also be revealed by mapping to the cavity photon statistics.[20] However, the double excitation dynamics modified by cavity modes have not been explored in detail.[22] This is critical to understand many nonlinear phenomena.

Multidimensional spectroscopic techniques provide an effective tool for probing the structure and dynamics of excitons in molecular aggregates,[27–32] including the excitonic energy transfer in light-harvesting complexes (LHCs).[33–37] Most efforts were devoted to single-exciton transport and its dependence on the intra-molecular as well as inter-molecular interactions and the energetic disorder of the chromophores.[38,39,41–44] The dissipating excitation energy in these excitonic aggregates includes desired quenching mechanism[45,46] and exciton-exciton annihilation (EEA)[47–49] in the double-exciton states which however are less studied.[40]

Light-harvesting complex II (LHCII), one of the most abundant (>50%) antenna complexes in plants, is the primary energy harvesting component of the pigment-protein assembly that participates in funneling the absorbed photon to the reaction center Photosystem (PSII) to initiate the charge separation. This photosynthetic process in high green plants had attracted much attention since the 4 Å-resolved crystallographic structure of the major light-harvesting complex II (LHCII) has been reported.[50,51] The LHCII monomeric subunit modeled based on the X-ray-resolved structure in an icosahedral proteoliposome assembly at atomic detail shows 14 chlorophylls (Chls) distinguished as 8 Chla and 6 Chlb molecules.[84] Recent spectroscopic studies revealed long-lasting quantum coherence in photosynthetic complexes with a timescale of 500 fs.[33–37] Much theoretical research work had focused on the quantum nature of energy transport in these complexes.[38,39,41,52–59] The excitonic coherence demonstrated in LHCII[60] and its dephasing rate were measured by coherence-specific polarization sequence in two-dimensional electronic spectroscopy.[61] The role of quantum coherence is still under debate.[62–64] The influence of protein environments in both LHCII and Fenna-Matthews-Olson (FMO) complex[17,27,70–79] was investigated by multidimensional spectroscopy.[65–69] Despite these achievements, the relaxation processes of higher excitations in photosynthetic complexes has not been explored in detail,[75,76] due to the lack of adequate spectroscopic technique for accessing the two-exciton band.

In this computational study, we show how the relaxation dynamics in the single and double excitation manifolds of LHCII antenna may be revealed by using time-and-frequency resolved photon coincidence counting spectroscopy.[80–82] This is a four-dimensional technique provided by two time and two frequency control gates, which has been proposed to explore

[a)]Current address: Institute for Quantum Science and Engineering, Texas A&M University, College Station, Texas 77843, USA. Electronic mail: zhedong.zhang@tamu.edu.
[b)]Electronic mail: dorfmank@lps.ecnu.edu.cn
[c)]Current address: Theory Department, Max Planck Institute for the Structure and Dynamics of Matter, Luruper Chaussee 175, Hamburg 22761, Germany. Electronic mail: debnath.arunangshu@gmail.com.
[d)]Electronic mail: smukamel@uci.edu

polariton dynamics.[83] It is a challenge to resolve the excitation energy transfer pathways in LHCII, due to the large line-broadening. This scenario can be remedied by placing the complex in an optical cavity. We find that the hybrid nature of polaritons with strong exciton-photon interaction considerably modifies the energy transfer rates and pathways, which can be monitored by the temporal and spectral parameters of the gated detection.

II. THE MONOMERIC LHCII AGGREGATE

The 2.72 Å-resolved X-ray diffraction structure of LHCII antenna[84] (Fig. 1) shows three monomeric units embedded in the protein structures—all residing in the thylakoid membranes. The constituent 42 chlorophylls (14 in each monomer) are distinguished as types *a* (Chla) and *b* (Chlb). They can be further classified, depending on their specific orientation in thylakoid membranes, as belonging to stromal(8) and lumenal(6) layers. The network arrangement of Chla and Chlb plays a crucial role in the energy transfer occurring in the single exciton manifold. The structural assignments and kinetic roles of individual Chls were corroborated by extensive molecular dynamics simulations and simultaneous fits of Linear Absorption (LA), Transient Absorption (TA), and Circular Dichroism (CD) spectra.[21–24] However, the abstraction of a monomer from the full trimer aggregate is not easy, and the participation of some of the Chla sites in the excitonic network is under debate.[25] The site dipoles were assigned at the Mg center of individual porphyrin rings in each chlorophyll, allowing us to model the monomer as the configuration of 14 sites with their respective site dipoles properly oriented, shown in Fig. 1 (left). The Frenkel exciton Hamiltonian of the monomeric LHCII is of the form

$$H_{ex} = E_\Omega |\Omega\rangle\langle\Omega| + \sum_{m=1}^{N} \varepsilon_m b_m^\dagger b_m + \sum_{\substack{(m,n)\\ m\neq n}} t_{mn}(b_m^\dagger b_n + b_n^\dagger b_m) + \sum_{m=1}^{N} U_m b_m^\dagger b_m^\dagger b_m b_m, \quad (1)$$

where $N = 14$ and b_m's are bosonic annihilation operators representing the excitons. Ω denotes the ground electronic state. ε_m's are the onsite energies of both Chla and Chlb. t_{mn} is the dipole-dipole interaction between chlorophylls m and n. U_m describes the onsite anharmonicity, which causes the exciton-exciton scattering. Here we only take into account onsite scattering because of its dominating contribution in many-body interaction in several aggregates.[21,22,85] Novoderezkin *et al.*[21,22,85] showed that in a LHCII monomer the $S_1 - S_2$ transition of chlorophyll is 100 cm^{-1} blue-shifted with respect to the $S_0 - S_1$ transition. The site energies were taken as adjustable parameters fitted to the absorption spectrum, which shows the consistence with Renger's previous work on LHCII by means of the first-principle simulation.[26] The dipole-dipole couplings were obtained from Ref. 23 while the site dipole strengths were taken to be 3.74 D and 3.19 D for Chla and Chlb, respectively. The matrix of dipole moments including the two-exciton states is directly constructed through the operator $\mu = \sum_{m=1}^{14} \mu_m(b_m + b_m^\dagger)$, where μ_m is the transition dipole between ground and single-exciton states on each site. This suggests that $U_m \simeq 50$ cm^{-1}. In LHCII, the structure-function relationships become more interesting due to symmetric orientations and dense packing of pigments compared to the bacterial antenna, e.g., <1 nm distance between individual Chls. Although intra-site couplings give rise to delocalized excited states, the variance of the local couplings across sites leads to a coexistence of weakly and strongly coupled energy acceptor pigments. This results in an interplay between local and nonlocal excitations as well as a competition between energy transport and exciton-exciton annihilation (EEA) mechanisms.

III. THE LHCII ANTENNA IN AN OPTICAL CAVITY

We place the monomeric LHCII in a single-mode optical cavity with the photon Hamiltonian

$$H_\gamma = \hbar\omega_c a^\dagger a \quad (2)$$

and a is the photon annihilation operator. The dipolar exciton-photon interaction under rotating-wave approximation takes the form

$$H_{ex-cav} = \sum_{m=1}^{N} g_m(b_m^\dagger a + b_m a^\dagger), \quad (3)$$

where g_m is the coupling strength between matter and photons, which can be experimentally varied by means of the control of the incident beam or cavity size.[18] In the simulation as shown later, we simply assume the identical g for all the sites in LHCII antenna. The total Hamiltonian of the joint system (aggregate + photon) is

$$H_S = H_{ex} + H_\gamma + H_{ex-cav} \quad (4)$$

which conserves the number of excitations $M = \sum_{m=1}^{N} b_m^\dagger b_m + a^\dagger a$. Here $M = 0, 1, 2$ will be applied when calculating the

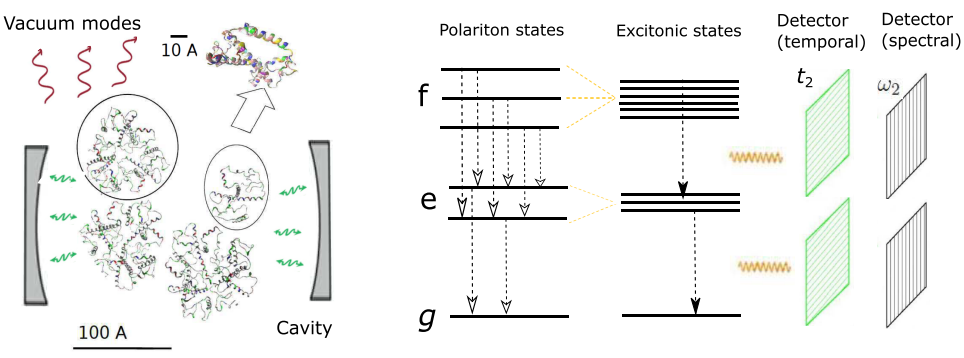

FIG. 1. (Left) LHCII aggregate from spinach. (Right) Sketch of the temporal-and-spectral-resolved photon coincidence signal in a microcavity.

energy spectrum of the complex. Let $|e_n\rangle$, $|f_l\rangle$ denote the polariton states of the joint system with respect to the single- and double-excitation bands. The total Hamiltonian can be recast in a diagonal form

$$H_S = E_\Omega |\Omega\rangle\langle\Omega| + \sum_{\sigma=e}^{f}\sum_{n=1}^{D_a} \hbar\omega_n^\sigma |\sigma_n\rangle\langle\sigma_n|, \tag{5}$$

where $|\sigma_n\rangle = \sum_{m=1}^{D_\sigma} O_{nm}^{(\sigma),T}|\phi_m^{(\sigma)}\rangle$; $n = 1,2,\ldots,D_\sigma; \sigma = e,f$. $O^{(a)}$ are the orthogonal matrices diagonalizing H_S in the e and f blocks, with $D_e = 15$, $D_f = 120$ states, respectively. Notice that $|\phi_m^{(e)}\rangle$ and $|\phi_m^{(f)}\rangle$ stand for the site basis (localized) for single- and double-excitations, respectively. $|O_{nm}^{(\sigma),T}|^2$ are the g_m-dependent mixing coefficients describing the relative excitonic and photonic weightings of the polariton states.

IV. REDFIELD EQUATIONS FOR POLARITON RELAXATION

Nuclear motions cause the excitonic dephasing and line broadening. Here we assume a harmonic bath for the nuclear motions, and the interaction between excitons and vibrations is

$$H_{ex-vib} = \sum_{m=1}^{N}\sum_{s} \lambda_{m,s} b_m^\dagger b_m \left(B_s^{(m)} + B_s^{(m),\dagger}\right), \tag{6}$$

where $B_s^{(m)}$ are bosonic annihilation operators and the index s runs over the high-frequency vibration and low-frequency phonon modes. The reorganization energy $\lambda_{m,s}$ gives the coupling strength of individual molecules to these modes and we further assume the spectral densities

$$J_m(\omega) = \frac{\pi}{\hbar}\sum_s \lambda_{m,s}^2 \delta(\omega - \nu_s^{(m)}). \tag{7}$$

To study the relaxation process in LHCII antenna, we have to specify the spectra density $J(\omega)$, which has been constructed by fitting of fluorescence line-narrowing (FLN) at 77 K.[21,86,87] The spectral density includes 48 high-frequency modes with frequencies ω_j describing the coupling to high-frequency vibration of nucleus and an overdamped Brownian mode describing the coupling to low-frequency phonons

$$J_m(\omega) = 2\lambda_0 \frac{\omega\gamma_0}{\omega^2+\gamma_0^2} + \sum_{i=1}^{48} 2\lambda_i\omega_i^2 \frac{\omega\gamma_i}{(\omega^2-\omega_i^2)^2+\omega^2\gamma_i^2} \tag{8}$$

which is plotted in Fig. 2 (top) with the parameters given in Fig. 2 (bottom) and $\lambda_j = S_j\omega_j$. $\lambda_0 \simeq 37\ \mathrm{cm}^{-1}$ and λ_j are termed as reorganization energies induced by phonons and vibrations. $\gamma_0 \simeq 30\ \mathrm{cm}^{-1}$ is the Debye cutoff frequency of low-frequency phonons and $\gamma_j \simeq 3\ \mathrm{cm}^{-1}$ describes the lifetime of those high-frequency vibrations.[22] We recast the exciton number operators $b_m^\dagger b_m = \sum_{\sigma=e}^{f}\sum_{l=1}^{D_\sigma} V_l^{m,\sigma}|\phi_l^{(\sigma)}\rangle\langle\phi_l^{(\sigma)}|$ in terms of polariton states

$$b_m^\dagger b_m = \sum_{\sigma=e}^{f}\sum_{l=1}^{D_\sigma}\sum_{p=1}^{D_\sigma} G_{lp}^{m,\sigma}|\sigma_l\rangle\langle\sigma_p| \tag{9}$$

and $G_{lp}^{m,\sigma} = \sum_{r=1}^{D_\sigma} O_{lr}^{(\sigma),T} V_r^{m,\sigma} O_{rp}^{(\sigma)}$. By neglecting the system-reservoir entanglement, the total density matrix takes the

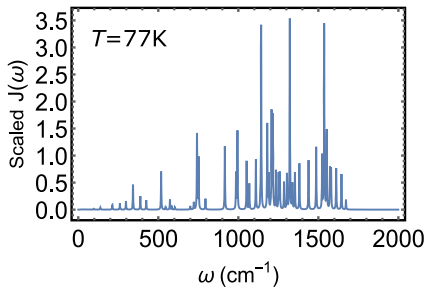

ω_j	S_j	ω_j	S_j	ω_j	S_j
97	0.02396	752	0.02578	1286	0.00454
138	0.02881	795	0.00485	1304	0.00576
213	0.03002	916	0.02123	1322	0.03032
260	0.02669	986	0.01031	1338	0.00394
298	0.02669	995	0.02274	1354	0.00576
342	0.06035	1052	0.01213	1382	0.00667
388	0.02487	1069	0.00636	1439	0.00667
425	0.01486	1110	0.01122	1487	0.00788
518	0.03942	1143	0.04094	1524	0.00636
546	0.00269	1181	0.01759	1537	0.02183
573	0.00849	1190	0.00667	1553	0.00909
585	0.00303	1208	0.01850	1573	0.00454
604	0.00194	1216	0.01759	1580	0.00454
700	0.00197	1235	0.00697	1612	0.00454
722	0.00394	1252	0.00636	1645	0.00363
742	0.03942	1260	0.00636	1673	0.00097

FIG. 2. (Top) Spectral density $J_m(\omega)$ where the contribution from high-frequency vibrational modes is reflected by those sharp peaks. (Bottom) Values of frequencies and Huang-Rhys factors ω_j (cm^{-1}), $S_j; j = 1,2,\ldots,48$ obtained from fluorescence line-narrowing (FLN).[21,86]

form $\rho_{s+b}(t) = \rho(t)\otimes\prod_{j=1}^{N}\rho_{R_j}(0)$, where the high-frequency vibrations and phonons are at thermal equilibrium: $\rho_{R_j}(0) = Z_j^{-1}\prod_s e^{-\beta\hbar\nu_s B_s^{(j),\dagger}B_s^{(j)}}$, $\beta = \frac{1}{k_B T}$, and $T = 77$ K is the temperature of the environment surrounding the complex. After tracing out the vibrational and phonon degrees of freedom, the relaxation dynamics of LHCII placed in an optical cavity is governed by the reduced density matrix of polaritons obeying the Markovian quantum master equation (QME). Making the secular approximation which decouples the population and coherence dynamics, the QME is recast into the Lindblad form

$$\frac{\mathrm{d}\rho}{\mathrm{d}t} = \frac{i}{\hbar}[\rho, H_S] + \sum_{\substack{\sigma=e\\ \sigma'=e}}^{f}\sum_{l=1}^{D_\sigma}\sum_{p=1}^{D_{\sigma'}}\sum_{l'=1}^{D_{\sigma'}}\left(\Gamma_{lp,l'p'}^{(\sigma,\sigma')} + \Gamma_{p'l',pl}^{(\sigma',\sigma)}\right) \times\left(C_{lp}^{(\sigma)}\rho\, C_{p'l'}^{(\sigma'),\dagger} - \frac{1}{2}\left\{C_{p'l'}^{(\sigma'),\dagger}, C_{lp}^{(\sigma)}\rho\right\}\right), \tag{10}$$

where $\Gamma_{lp,l'p'}^{(\sigma,\sigma')} = \sum_{m=1}^{N} G_{lp}^{m,\sigma} G_{l'p'}^{m,\sigma'}\gamma_m(\omega_l^\sigma - \omega_p^\sigma)$ and $C_{lp}^{(\sigma)} = |\sigma_l\rangle\langle\sigma_p|$ is the transition operator. The damping rate reads $\gamma_m(\omega) = \int_0^\infty d\nu\, J_m(\nu)[n_\nu^T\delta(\omega-\nu) + (n_\nu^T+1)\delta(\omega+\nu)]$ with the bosonic occupation $n_\nu^T = [\exp(\hbar\nu/k_BT)-1]^{-1}$. We get

$$\gamma_m(\omega) = \begin{cases} J_m(\omega)n_\omega^T & (\omega > 0),\\ \dfrac{2\lambda_0 k_B T}{\hbar\gamma_0} + \sum_{j=1}^{48}\dfrac{2\lambda_j\gamma_j k_B T}{\hbar\omega_j^2} & (\omega = 0),\\ J_m(|\omega|)\left(n_{|\omega|}^T + 1\right) & (\omega < 0). \end{cases} \tag{11}$$

We shall recast the QME in Liouville space $\partial_t|\rho\rangle\!\rangle = \hat{L}|\rho\rangle\!\rangle$, $|\rho\rangle\!\rangle = |\rho_{pop}\rangle\!\rangle \oplus |\rho_{coh}\rangle\!\rangle$. The secular approximation introduced

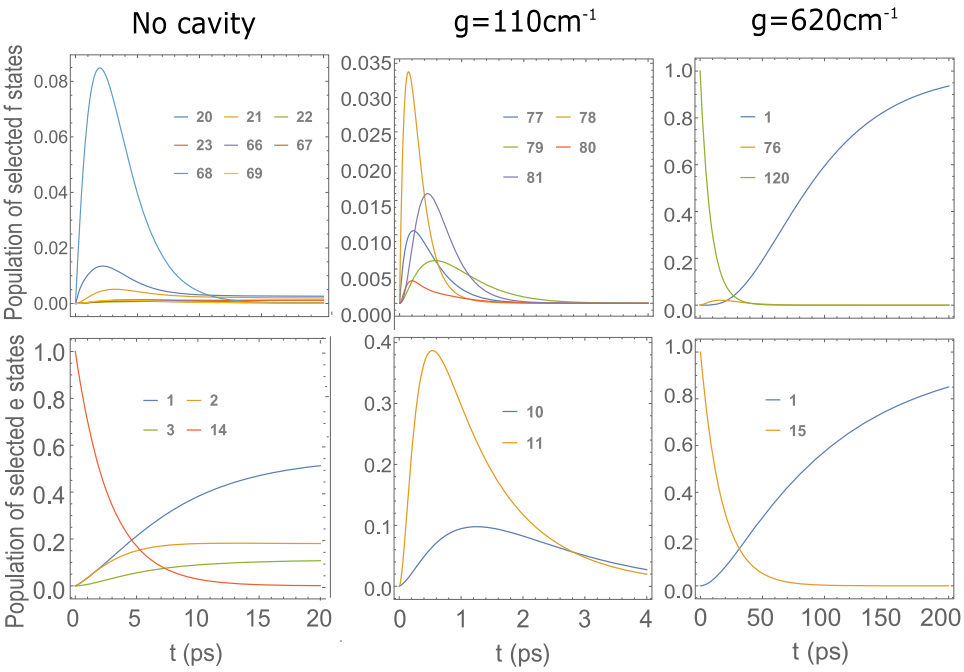

FIG. 3. Population dynamics of selected states as resolved by the peaks in photon-coincidence counting spectra shown later. (Top row) Double excitations, (bottom row) single excitation; (left column) without cavity, (middle column) $g = 110$ cm^{-1}, (right column) $g = 620$ cm^{-1}.

in Eq. (10) decouples the populations $|\rho_{pop}\rangle\!\rangle$ and coherences $|\rho_{coh}\rangle\!\rangle$, which leads to the block diagonal form $\hat{L}$: $\hat{L} = \hat{L}_{pop} \oplus \hat{L}_{coh}$, where these two terms govern the dynamics of population and coherence, respectively. The matrix elements of the Liouvillians $\hat{L}_{pop}$ and $\hat{L}_{coh}$ are determined by Eq. (10) and the details are given in the Appendix.

The time-resolved polariton population has been calculated by numerical solution of the QME in Eq. (10). For f-band, assuming that the system is initially prepared at the highest level the polariton population then reads $|P^{(f)}(t)\rangle\!\rangle = \exp(\hat{L}^{(f)}_{pop}t)|f_{h_2}, f_{h_2}\rangle\!\rangle$, where $h_2 = 120$ and $h_2 = 105$ for the cases with and without optical cavity, respectively. For e-band, the polariton population reads $|P^{(e)}(t)\rangle\!\rangle = \exp(\hat{L}^{(e)}_{pop}t)|e_{h_1}, e_{h_1}\rangle\!\rangle$ by assuming that the system is initially prepared at the highest singly excited state. Notice that $h_1 = 15$ and $h_1 = 14$ for the cases with and without optical cavity, respectively. $\hat{L}^{(\sigma)}_{pop}$; $\sigma = e,f$ denotes the population blocks in the Liouvillian $\hat{L}$. The parameters of the 14-site LHCII monomer are obtained from Refs. 22 and 85. The fundamental frequency of cavity photon is tuned to be $\omega_c = 15\,200$ cm^{-1}.

Figure 3 (top) displays the f-band population dynamics of some selected exciton and polariton states, while Fig. 3 (bottom) shows the population dynamics of e-band. The states are picked up as the ones resolved by the peaks in photon-coincidence counting spectroscopy as explained later on. It is worth noticing that the cavity photons accelerate both the f- and e-band relaxation dynamics in medium exciton-photon coupling regime, while they considerably suppress the relaxation dynamics in strong exciton-photon coupling regime. This is due to the fact that the large energy splitting of ~4000 cm^{-1} between polariton states that is off-resonant with the frequency of vibrational modes leads to the screening of the dissipation from the high-frequency vibrations. We will further discuss this issue in detail when presenting the photon-coincidence counting signal.

V. THE ABSORPTION SPECTRUM

Based on the linear response theory, the absorption spectrum plotted in Fig. 4 was the imaginary part of the response function and was calculated from the QME (10)

$$\tilde{\chi}^{(1)}(\omega) = \frac{1}{\pi}\sum_{p=1}^{D_e}\frac{\mu^2_{ge_p}|\mathrm{Re}(L^{coh}_{ge_p,ge_p})|}{(\omega-\omega^e_p)^2 + |\mathrm{Re}(L^{coh}_{ge_p,ge_p})|^2}, \qquad (12)$$

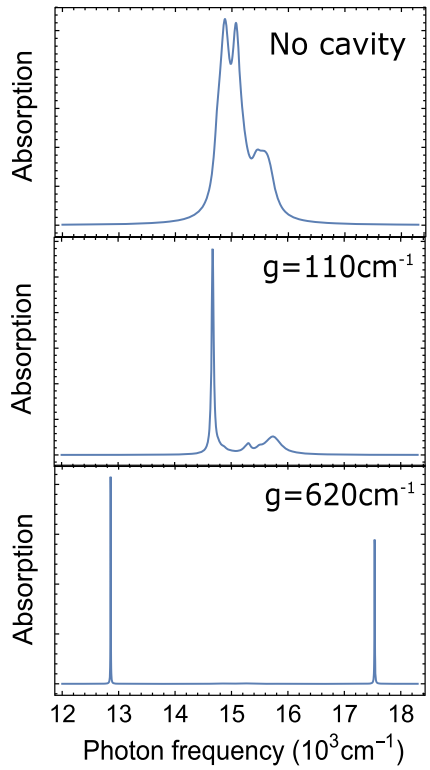

FIG. 4. Absorption spectra of LHCII with no cavity (top), intermediate coupling strength $g = 110$ cm^{-1} (middle), and strong coupling strength $g = 620$ cm^{-1} (bottom).

where $L^{coh}_{ge_p,ge_p}$ is the element of Liouvillian in the coherence block. Notice that the vacuum-induced radiative linebroadening is not included hereafter. This is due to the fact that the lifetime caused by spontaneous emission of electronic excitation in optical regime is of the order of ns, which contributes a much narrower linewidth than the one of ps given by the molecular vibrations in LHC aggregate. Figure 4 elucidates the two polariton branches in singly excited states in strong exciton-photon coupling regime. The large exciton dephasing rate caused by vibrations smears out the frequency resolution, as reflected by the broaden peaks in Fig. 4 (top) without cavity. The suppression of dephasing results in the narrow linewidth as the coupling to photon modes is increased.

VI. THE PHOTON COINCIDENCE COUNTING SIGNAL

The photon statistics offers a powerful spectroscopic technique for probing matter properties. The atoms in detector are promoted from ground state a to the ionized continuum represented by manifold b, by absorbing the photons. Meanwhile the photon detection brings the field from its initial state p_i to finial state p_f. The transition amplitude at time t for such processes can be calculated by first-order time-dependent perturbation theory

$$A_\gamma \propto \langle b|\mathbf{d}|a\rangle \cdot \left\langle p_f|\mathbf{E}_v(t)|p_i\right\rangle, \tag{13}$$

where $\mathbf{d}$ denotes the dipole moment of the atoms in the detector. The photon absorption determines the output of the detector which is proportional to the modulus square of the transition amplitude given in Eq. (13). Since all possible final states need to be considered, the photon absorption is given by

$$T_\gamma \propto \sum_i \sum_f \rho_i \left|\left\langle p_f|\mathbf{E}_v(t)|p_i\right\rangle\right|^2 = \mathrm{Tr}\left[\rho \mathbf{E}_v^\dagger(t)\cdot\mathbf{E}_v(t)\right] \tag{14}$$

and $\mathbf{E}_v(t) = \mathbf{E}_v(t)^{(-)} + \mathbf{E}_v^{(+)}(t)$ with

$$\mathbf{E}_v(t)^{(-)} = \sum_{s,\lambda}\sqrt{\frac{2\pi\omega_{s,\lambda}}{\mathrm{V}}}\,\hat{\epsilon}_{s,\lambda}a_{s,\lambda}e^{i(\mathbf{k}_s\cdot\mathbf{r}-\omega_{s,\lambda})t} \tag{15}$$

being the negative-frequency part of the vacuum field. $\mathbf{E}_v^{(+)} = \left(\mathbf{E}_v^{(-)}\right)^\dagger$. Note that the statistical average over the initial ensemble of the matter is carried out with the weight ρ_i. This is because we rarely know with certainty which initial state the system stays. Here we detect the vacuum photon modes emitted by the aggregates, rather than the photon emission from microcavities. The energy of vacuum modes detected is $H_v = \sum_{s,\lambda}\hbar\omega_{s,\lambda}a^\dagger_{s,\lambda}a_{s,\lambda}$. The interaction between polariton and vacuum modes reads $H_{pol-vac} = \mathbf{P}\cdot\mathbf{E}_v(t)$, where $\mathbf{P} = \sum_{i=x,y,z}\hat{\epsilon}_i(V_i + V_i^\dagger)$ is the polariton dipole moment and $V_i = \sum_{j=1}^{D_e}\mu^{(i)}_{ge_j}|g\rangle\langle e_j| + \sum_{q=1}^{D_e}\sum_{l=1}^{D_f}\mu^{(i)}_{e_qf_l}|e_q\rangle\langle f_l|$. The fabrication of high-quality microcavities with the Q-factor up to ~48 000 makes us able to omit the cavity damping at current stage.[90] We could also place the detectors off the cavity axis to eliminate the cavity leaking along that direction as illustrated in Fig. 1 (left), by assuming the small solid angle of the cavity mirrors.

We assume that the antenna is initially excited to the two-exciton manifold and the emitted cascades of two photons are then detected by time- and frequency-resolved photon coincidence. The coincidence signal is given by the four-point correlation function of emitted photons absorbed by the detectors[80,88]

$$g^{(2)}(t_1,\omega_1;t_2,\omega_2) = \langle \hat{n}_{t_1,\omega_1}\hat{n}_{t_2,\omega_2}\rangle \tag{16}$$

which gives rise to the second-order signal $S^{(2)}(t_1, \omega_1; t_2, \omega_2)$ and contains the information of the transition from f- to e-bands and the one from e-band to ground state, as illustrated in Fig. 1 (right). Such detection of the photon pairs is different from the single-photon statistics quantified by the two-point correlation function $g^{(1)}(t,\omega) = \langle\hat{n}_{t,\omega}\rangle$ which gives the first-order signal $S^{(1)}(t, \omega)$. In Eq. (16), $\hat{n}_{t_1,\omega_1}\hat{n}_{t_2,\omega_2} = \int dt''\hat{E}^\dagger_{t_1,\omega_1R}(t'')\hat{E}_{t_1,\omega_1L}(t'')\hat{E}^\dagger_{t_2,\omega_2R}(t'')\hat{E}_{t_2,\omega_2L}(t'')$. $\hat{E}_{t,\omega}(t'')$ is defined as the time-and-frequency-gated field operator, in terms of the bare field operator $\hat{E}(t)$ as $\hat{E}_{t,\omega}(t'') = \int_{-\infty}^{\infty}dt'F_f(t''-t',\omega)F_t(t',t)\hat{E}(t')$ and

$$F_f(t,\omega) = \frac{1}{2\pi}\int F_f(\omega',\omega)e^{i\omega' t}d\omega', \tag{17}$$

where the functions $F_t(t', t)$ centered at time t and $F_f(\omega', \omega)$ centered at frequency ω govern the time and spectral gates in the detectors, respectively. Using these time and spectral gate functions, we can calculate the $g^{(2)}$-function and obtain the signal

$$\begin{aligned}S^{(2)}(t_1,\omega_1;t_2,\omega_2) = &\int_{-\infty}^{\infty}\mathrm{d}t_1'\int_{-\infty}^{\infty}\mathrm{d}\tau_1\, D^{(1)}(t_1,\omega_1;t_1',\tau_1)\int_{-\infty}^{\infty}\mathrm{d}t_2'\int_{-\infty}^{\infty}\mathrm{d}\tau_2\, D^{(2)}(t_2,\omega_2;t_2',\tau_2)\\ &\times\sum_{s,s'}\sum_{r,r'}\langle\hat{E}^\dagger_{r'}(t_2'+\tau_2)\hat{E}^\dagger_{s'}(t_1'+\tau_1)\hat{E}_s(t_1')\hat{E}_r(t_2')\rangle_{\rho(t)},\end{aligned} \tag{18}$$

where $D^{(i)}(t_i,\omega_i;t_i',\tau_i) = \int d\omega''e^{-i\omega''\tau_i}|F_f(\omega'',\omega_i)|^2F_t^*(t_i'+\tau_i,t_i)F_t(t_i',t_i)$; $i = 1, 2$ are the time-domain detector spectrograms which control the photon countings for $f \to e$ and $e \to g$ transitions, respectively. $E_s(t)$ denotes the field operator of the emitted photons of mode s. Note that the correlation function of field E_s in Eq. (18) includes the average over the polarization orientation of emitted photons, which results in the factor $\left(\frac{4\pi}{3}\right)^4$. We have used the Lorentzian gates which give the resolution σ_T, σ_ω in time and frequency domains, respectively,

$$\begin{aligned}F_t(t',t) &= \theta(t'-t)e^{-\sigma_T(t'-t)}\\ F_f(\omega',\omega) &= \frac{i}{\omega'-\omega+i\sigma_\omega}\end{aligned}. \tag{19}$$

The time-domain detector spectrograms $D^{(i)}(t_i, \omega_i; t_i', \tau_i)$ are given in the Appendix. The connection between the photon counting signal and the matter response is obtained using a microscopic theory based on the perturbative series with respect to matter-vacuum interaction. The leading contribution to the signal comes from 4th-order expansion over the matter-vacuum coupling in Eq. (18), with the correlation function of matter $\langle \hat{\mathcal{T}} V_R^\dagger(t_2' + \tau_2) V_R^\dagger(t_1' + \tau_1) V_L(t_1') V_L(t_2') \rangle$,[80] where $\hat{\mathcal{T}}$ denotes the time-ordering and V is the lowering part of dipole moment that induces the transition to lower states. The subscripts L and R denote the multiplication from left and right sides, respectively, i.e., $V_L \rho = V\ \rho$, $V_R \rho = \rho V$. After some algebra we finally obtain for the photon counting coincidence

$$S^{(2)}(t_1, \omega_1; t_2, \omega_2) = 2 \sum_{n=1}^{3} \mathrm{Re}\left[S_i^{(n)} + S_{ii}^{(n)} \right] \tag{20}$$

with $S_i^{(n)}$, $S_{ii}^{(n)}$ given in the Appendix. The system is initially prepared in the doubly excited state $|\psi^{(f)}\rangle = \sum_{n=1}^{D_f} C_n^{(f)} |f_n\rangle$ where we took the highest-energy state $C_n = 0$ ($n = 1, 2, \ldots, D_f - 1$); $C_{D_f} = 1$.

Figure 5 shows the simulated correlated-photon counting signal $S^{(2)}(t_1, \omega_1; t_2, \omega_2)$ for different cavity coupling strength. Different gate parameters were used: (1) in top row, we simultaneously opened the t_1, t_2 gates for resolving the f-band relaxation and (2) in bottom row, we opened the t_2-gate initially and the t_1-gate with a time delay $t_1 - t_2$, for resolving the e-band relaxation. The figure elucidates that the cavity photons can greatly improve the frequency resolution, revealing the energy transfer pathways more clearly. This is due to the cavity-photon-induced suppression of dephasing and large energy splitting in polariton states, as will be discussed in detail later. The coupling to cavity photons further considerably slows down the relaxation dynamics in LHCII monomer and we will elaborate this point later on.

We have simulated the two-photon counting signal $S^{(2)}(t_1, \omega_1; t_2, \omega_2)$ with no optical cavity. The control of spectral and temporal gates helps monitoring the relaxation dynamics of excitons. To resolve the dynamics in f band, we set $t_1 = t_2$ and vary t_2. In Fig. 6, the anti-diagonal dashed lines denote the double excitation energies where $\omega_1 + \omega_2 = E_v^f$. The complex is initially prepared at the highest f state $|f_{105}\rangle\langle f_{105}|$, which results in the peak at $\omega_1 + \omega_2 = E_{105}^f$ for $t_1 = t_2 = 0$. By controlling t_2 through the temporal gate, we observe the extra peaks and their displacement. At $t_1 = t_2 = 1.5$ ps, 3 peaks can be resolved at $\omega_1 + \omega_2 \simeq 31\,400\ \mathrm{cm}^{-1}$, $30\,375\ \mathrm{cm}^{-1}$, $29\,825\ \mathrm{cm}^{-1}$, corresponding to the states $|f_{105}\rangle\langle f_{105}|$, $|f_{67}\rangle\langle f_{67}|$, $|f_{22}\rangle\langle f_{22}|$. At longer times, the peak centered at $\omega_1 + \omega_2 \simeq 30\,375\ \mathrm{cm}^{-1}$ vanishes ($t_1 = t_2 = 2.4$ ps) and the peak at $\omega_1 + \omega_2 \simeq 29\,825\ \mathrm{cm}^{-1}$ moves to $\omega_1 + \omega_2 \simeq 29\,600\ \mathrm{cm}^{-1}$ ($t_1 = t_2 = 20$ ps). By setting $t_2 = 0$ the f-band relaxation is blocked in the signal, as seen in Fig. 7. By controlling t_1 we observe in Fig. 7 the peak migration from $\omega_1 \simeq 15\,650\ \mathrm{cm}^{-1}$, $\omega_2 \simeq 15\,725\ \mathrm{cm}^{-1}$ to $\omega_1 \simeq 14\,825\ \mathrm{cm}^{-1}$, $\omega_2 \simeq 15\,725\ \mathrm{cm}^{-1}$ during ~5 ps, which is consistent with the previous pump-probe results.[21,22] This peak displacement in two temporal-gate control schemes agrees well with the population dynamics shown in the left column of Fig. 3 and seems to resolve the energy transfer paths in LHCII: $f_{105} \rightarrow$ (states f_{67}, f_{22} and their vicinities) $\rightarrow f_1, e_{14} \rightarrow (e_3, e_2, e_1)$ in doubly excited and singly excited manifolds, respectively. However, the pathways may not be clearly resolved due to the line broadening caused by large dephasing as illustrated in Fig. 6. On the other hand, the high density of f states as calculated by the energetic spectrum also results in poorly resolved peaks. The large broadening has already been illustrated in the absorption spectra depicted in Fig. 4 (top) where only two broad peaks can be resolved that represent the 14 singly excited states.

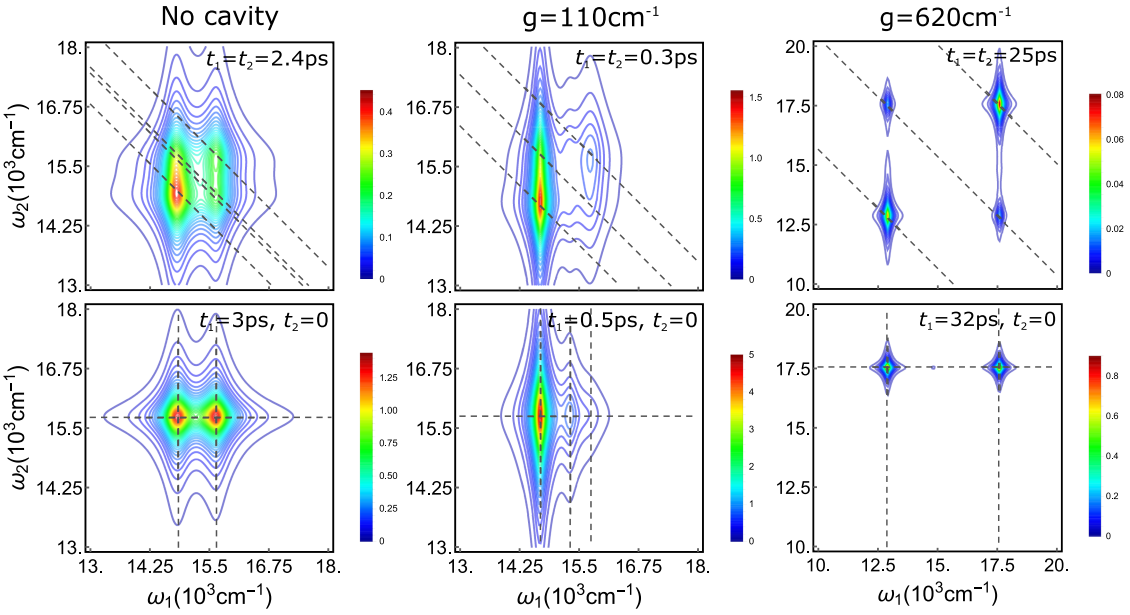

FIG. 5. 2D frequency-frequency correlation spectrum $S^{(2)}(t_1, \omega_1; t_2, \omega_2)$ with different schemes of gate parameters. (Left) No cavity, (middle) intermediate coupling to cavity $g = 110\ \mathrm{cm}^{-1}$, and (right) strong coupling to cavity $g = 620\ \mathrm{cm}^{-1}$. Gate parameters are (left) $\sigma_{\omega_1} = 10\ \mathrm{cm}^{-1}$, $\sigma_{\omega_2} = 10\ \mathrm{cm}^{-1}$, $\sigma_{T_1} = 93\ \mathrm{cm}^{-1}$, $\sigma_{T_2} = 200\ \mathrm{cm}^{-1}$; (middle) $\sigma_{\omega_1} = 10\ \mathrm{cm}^{-1}$, $\sigma_{\omega_2} = 10\ \mathrm{cm}^{-1}$, $\sigma_{T_1} = 93\ \mathrm{cm}^{-1}$, $\sigma_{T_2} = 360\ \mathrm{cm}^{-1}$; (right) $\sigma_{\omega_1} = 10\ \mathrm{cm}^{-1}$, $\sigma_{\omega_2} = 10\ \mathrm{cm}^{-1}$, $\sigma_{T_1} = 93\ \mathrm{cm}^{-1}$, $\sigma_{T_2} = 150\ \mathrm{cm}^{-1}$.

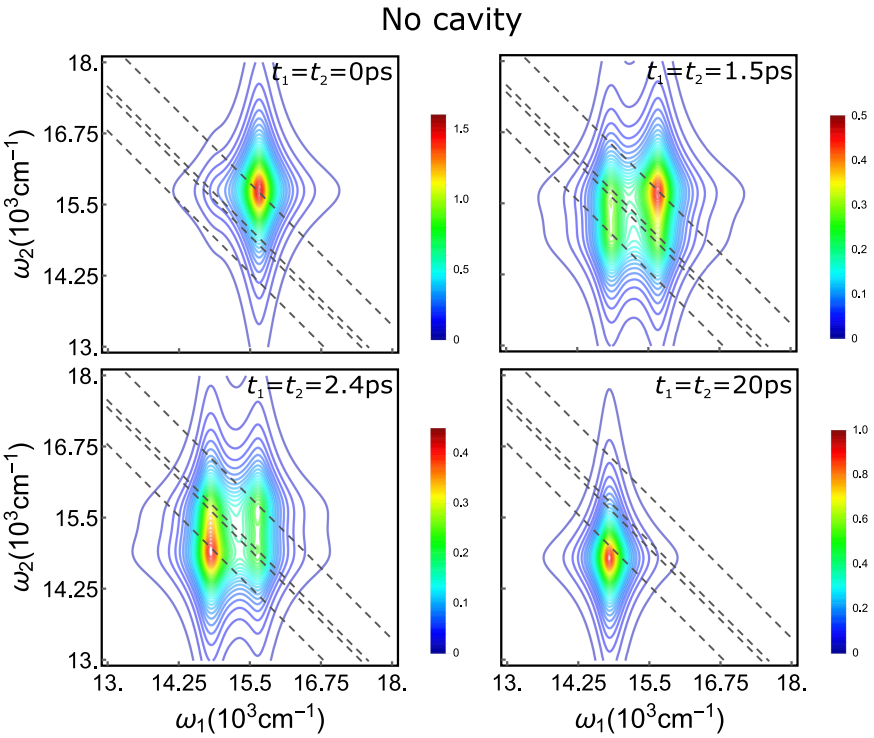

FIG. 6. 2D frequency-frequency correlation spectrum $S^{(2)}(t_1, \omega_1; t_2, \omega_2)$ without cavity where $t_1 = t_2$; the anti-diagonal dashed lines denote $\omega_1 + \omega_2$ = 31 400 cm^{-1}, 30 375 cm^{-1}, 29 825 cm^{-1}, 29 600 cm^{-1}. Gate parameters are σ_{ω_1} = 10 cm^{-1}, σ_{ω_2} = 10 cm^{-1}, σ_{T_1} = 93 cm^{-1}, σ_{T_2} = 200 cm^{-1}.

Monitoring the energy transfer pathways in LHCII antenna is therefore a difficult challenge.

High-quality optical cavities can overcome this difficulty by observing polaritons rather than excitons. To this end, we have simulated the photon-coincidence counting signal in different coupling regimes to the optical cavity. Here we will ignore the cavity damping which indicates longer lifetime of photons than excitons. This regime has been achieved in recent experiments with a high-Q factor up to 48 000 for optical microcavities.[90] Figure 8 illustrates the frequency-frequency correlation spectra $S^{(2)}(t_1, \omega_1; t_2, \omega_2)$ for intermediate exciton-photon interaction with $t_1 = t_2$ in order to reveal the f-band relaxation. The relaxation rate in the cavity becomes faster than the case without cavity. In particular, the energy migrates in 0.3 ps from f_{120} to the vicinity of f_{80} with energy around 30 430 cm^{-1}, as shown by the peak displacement from $\omega_1 + \omega_2$ $\simeq$ 31 525 cm^{-1} to $\omega_1 + \omega_2 \simeq$ 30 440 cm^{-1}. During the following 0.5 ps, the peak moves from $\omega_1 + \omega_2 \simeq$ 30 440 cm^{-1}

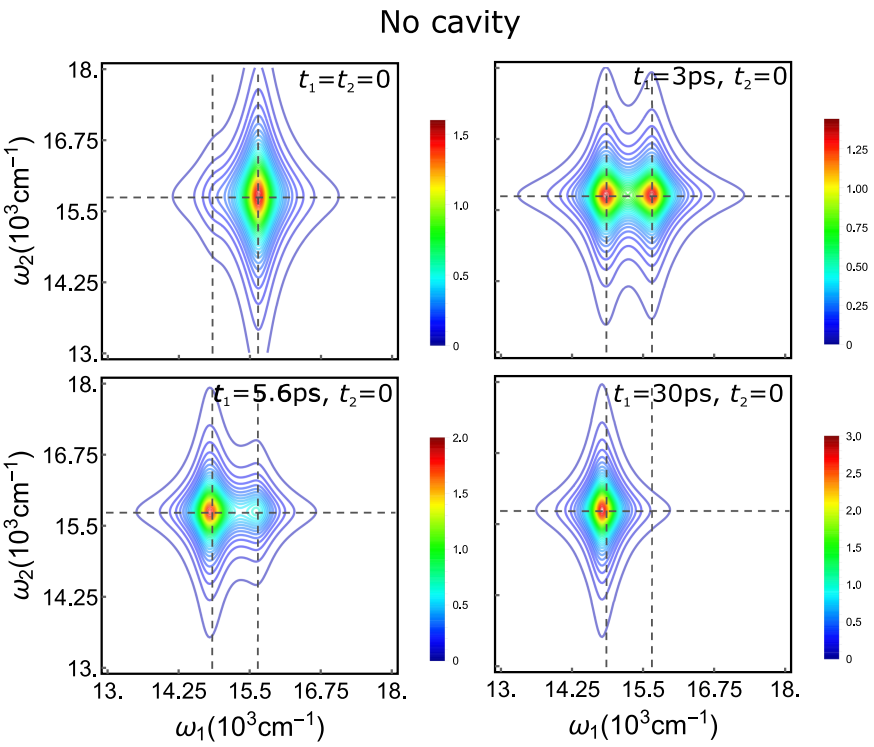

FIG. 7. 2D frequency-frequency correlation spectrum $S^{(2)}(t_1, \omega_1; t_2, \omega_2)$ without cavity where $t_2 = 0$; the vertical and horizontal dashed lines denote ω_1 = 15 650 cm^{-1}, 14 850 cm^{-1}, and ω_2 = 15 725 cm^{-1}, respectively. Gate parameters are σ_{ω_1} = 10 cm^{-1}, σ_{ω_2} = 10 cm^{-1}, σ_{T_1} = 93 cm^{-1}, σ_{T_2} = 200 cm^{-1}.

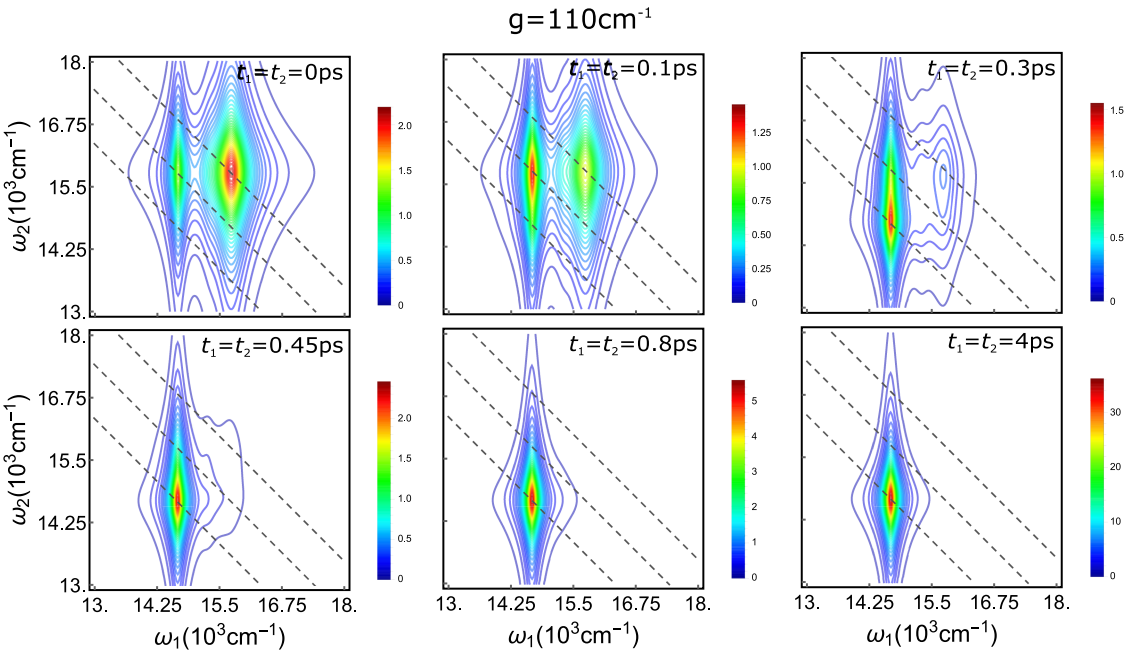

FIG. 8. 2D frequency-frequency correlation spectrum $S^{(2)}(t_1, \omega_1; t_2, \omega_2)$ for $t_1 = t_2$ in the regime of intermediate exciton-photon coupling $g = 110\ \mathrm{cm}^{-1}$; the anti-diagonal dashed lines denote $\omega_1 + \omega_2 = 31\,525\ \mathrm{cm}^{-1}$, $30\,440\ \mathrm{cm}^{-1}$, $29\,375\ \mathrm{cm}^{-1}$. Gate parameters are $\sigma_{\omega_1} = 10\ \mathrm{cm}^{-1}$, $\sigma_{\omega_2} = 10\ \mathrm{cm}^{-1}$, $\sigma_{T_1} = 93\ \mathrm{cm}^{-1}$, $\sigma_{T_2} = 360\ \mathrm{cm}^{-1}$.

to $\omega_1 + \omega_2 \simeq 29\,375\ \mathrm{cm}^{-1}$. By setting $t_2 = 0$ the f-band relaxation would not be detected, as displayed in Fig. 9. This indicates energy transport from states in the vicinity of f_{80} to f_1. This peak migration is in agreement with the population dynamics $\rho_{f_1}(t)$, $\rho_{f_{77}}(t)$, $\rho_{f_{78}}(t)$, $\rho_{f_{79}}(t)$, $\rho_{f_{80}}(t)$, $\rho_{f_{81}}(t)$ as depicted in the middle column of Fig. 3. By controlling the time gate t_1 we can alternatively observe in Fig. 9 the peak displacement from $\omega_1 = 15\,745\ \mathrm{cm}^{-1}$ in such a pathway that $\omega_1 = 15\,745\ \mathrm{cm}^{-1} \rightarrow 15\,310\ \mathrm{cm}^{-1} \rightarrow 14\,680\ \mathrm{cm}^{-1}$, keeping $\omega_2 = 15\,780\ \mathrm{cm}^{-1}$. This resolves the energy transfer pathway in the single excitation manifold $e_{15} \rightarrow (e_{10}, e_{11}) \rightarrow e_1$, which is consistent with the e-band population dynamics shown in Fig. 3 (middle). However, the large dephasing rate still results in line broadening shown in Figs. 8 and 9, which limits the resolution of the energy transfer pathways, especially in the f-band. The large dephasing is owing to the fact that energy

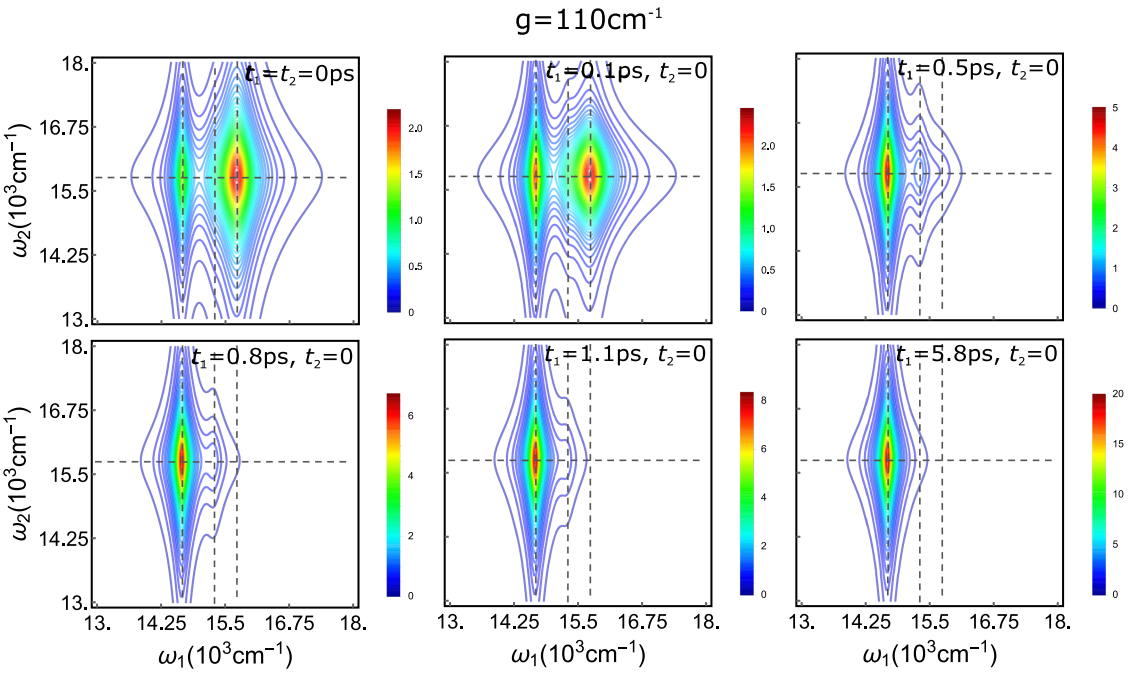

FIG. 9. 2D frequency-frequency correlation spectrum $S^{(2)}(t_1, \omega_1; t_2, \omega_2)$ for $t_2 = 0$ in the regime of intermediate exciton-photon coupling $g = 110\ \mathrm{cm}^{-1}$; the vertical and horizontal dashed lines denote $\omega_1 = 15\,745\ \mathrm{cm}^{-1}$, $15\,310\ \mathrm{cm}^{-1}$, $14\,673\ \mathrm{cm}^{-1}$, and $\omega_2 = 15\,780\ \mathrm{cm}^{-1}$, respectively. Gate parameters are $\sigma_{\omega_1} = 10\ \mathrm{cm}^{-1}$, $\sigma_{\omega_2} = 10\ \mathrm{cm}^{-1}$, $\sigma_{T_1} = 93\ \mathrm{cm}^{-1}$, $\sigma_{T_2} = 360\ \mathrm{cm}^{-1}$.

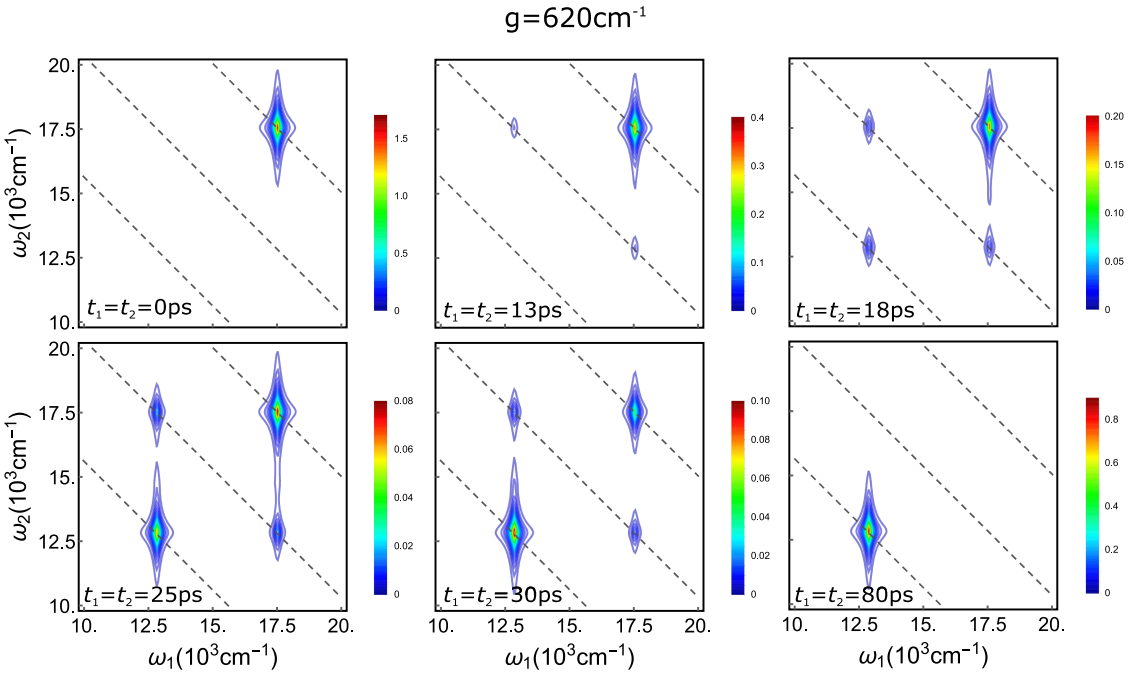

FIG. 10. 2D frequency-frequency correlation spectrum $S^{(2)}(t_1, \omega_1; t_2, \omega_2)$ for $t_1 = t_2$ in the regime of strong exciton-photon coupling g = 620 cm^{-1}; the anti-diagonal dashed lines denote $\omega_1 + \omega_2$ = 35 075 cm^{-1}, 30 400 cm^{-1}, 25 720 cm^{-1}, corresponding the three polariton branches. Gate parameters are σ_{ω_1} = 10 cm^{-1}, σ_{ω_2} = 10 cm^{-1}, σ_{T_1} = 93 cm^{-1}, σ_{T_2} = 150 cm^{-1}.

splitting still has the chance to be resonant with nuclear vibrations, despite the aggregate intermediately interacting with photons. We will see later that the strong exciton-photon interaction can change the whole scenario.

Figure 10 shows the frequency-frequency correlation spectra $S^{(2)}(t_1, \omega_1; t_2, \omega_2)$ in the strong exciton-photon coupling regime for $t_1 = t_2$. We use $g = 620$ cm^{-1} that exceeds the frequency detuning between excitons and photons, maximizing at ~440 cm^{-1}. There are three active polariton branches, according to the Dicke model.[89] The photon-coincidence counting spectra can resolve these 3 polariton states and their relaxation dynamics. In Fig. 10, we notice that the peak moves from $\omega_1 + \omega_2 \simeq 35\,075$ cm^{-1} to $\omega_1 + \omega_2 \simeq 30\,400$ cm^{-1} as well as $\omega_1 + \omega_2 \simeq 25\,720$ cm^{-1} in ~18 ps. Beyond ~25 ps, we

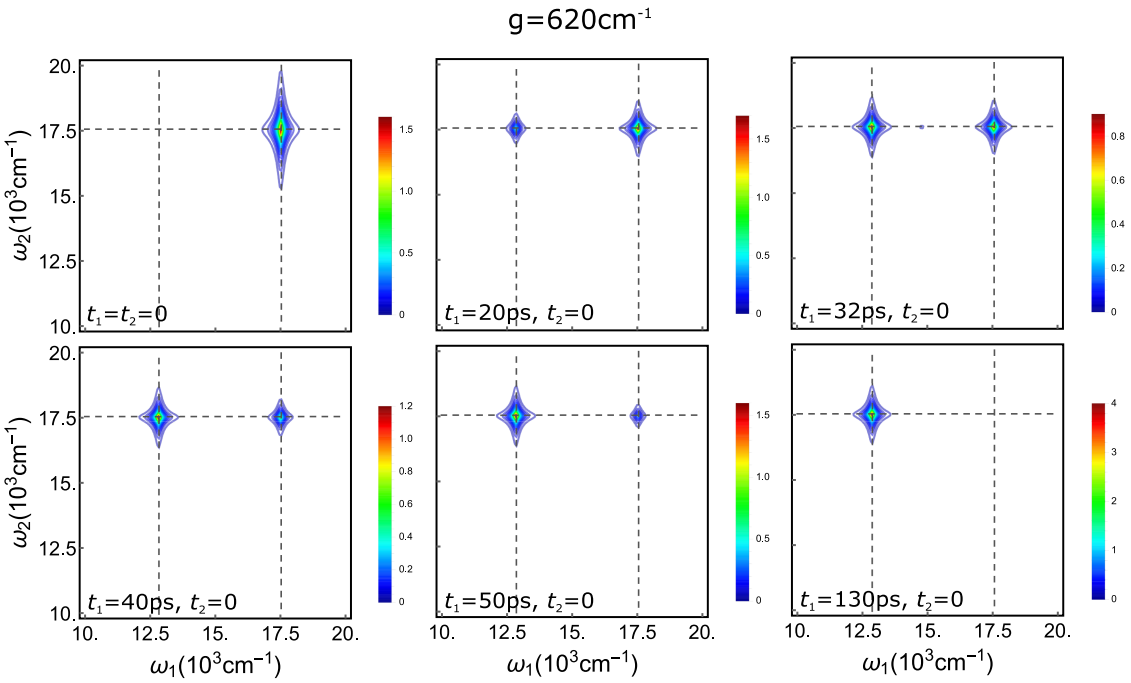

FIG. 11. 2D frequency-frequency correlation spectrum $S^{(2)}(t_1, \omega_1; t_2, \omega_2)$ for $t_2 = 0$ in the regime of strong exciton-photon coupling $g = 620$ cm^{-1}; the vertical and horizontal dashed lines denote ω_1 = 17 537 cm^{-1}, 12 859 cm^{-1}, and ω_2 = 17 539 cm^{-1}, respectively. Gate parameters are σ_{ω_1} = 10 cm^{-1}, σ_{ω_2} = 10 cm^{-1}, σ_{T_1} = 93 cm^{-1}, σ_{T_2} = 150 cm^{-1}.

see the migration of the peak centered at $\omega_1 + \omega_2 \simeq 30\,400$ cm^{-1} to $\omega_1 + \omega_2 \simeq 25\,720$ cm^{-1}. Alternatively by setting $t_2 = 0$ the f-band relaxation is masked when detecting the signal, as shown in Fig. 11 which clearly resolves the two polariton states in e-band. By controlling the time-gate t_1, we find peak shift from $\omega_1 = 17\,537$ cm^{-1} to $\omega_1 = 12\,859$ cm^{-1}, keeping $\omega_2 = 17\,539$ cm^{-1}. Referring to the population dynamics of polaritons in Fig. 3 (right), Fig. 10 clearly resolves the energy transfer in double excitation manifold during the first ~18 ps in such a way that the excitons migrate from upper-polariton-branch (UPB with energy of 35 076 cm^{-1}, f_{120}) to middle-polariton-branch (MPB with energy of 30 399 cm^{-1}, f_{76}) as well as lower-polariton-branch (LPB with energy of 25 719 cm^{-1}, f_1). The subsequent energy transport from UPB to LPB after $t_1 = t_2 \simeq 25$ ps is then resolved. Figure 11 illustrates the energy transfer from UPB to LPB in the single excitation manifold. These manifest that the relaxation rate of the complex is estimated to be $\gtrsim$20 ps, which is much larger than that without cavity. Figures 10 and 11 further show that the linewidth is much smaller than the energy splitting of polaritons, leading to a considerable improvement of resolution, compared to both the cases without and with intermediate coupling to cavity photons. This is attributed to the small dephasing of polariton states, as illustrated by the narrow peaks in linear absorption shown in Fig. 4 (right). In our parameter regime, the energy splitting $\Delta E_{pol} \simeq 2g\sqrt{N} \sim 4000$ cm^{-1} between polariton branches becomes off-resonant with the energy scale of high-frequency nuclear vibrations shown in the spectral density in Fig. 2, where N is the aggregate size. This reduces the vibration-produced dissipation and dephasing which serve as the origin for line broadening. In other words, the quantum coherence between excitons and photons produced by the strong interaction with quantized photon modes can enable the aggregate to overcome the large dephasing caused by nuclear vibrations. Thus the relaxation rate is considerably reduced as illustrated in Figs. 3 (right), 10, and 11. This indicates that the energy transport is considerably slowed down by strong coupling to the cavity photons.

VII. CONCLUSIONS

The energy transport processes in a monomeric LHCII aggregate placed in an optical cavity were investigated by coincidence counting of the photons emitted by the doubly excited complex. Because of the large dephasing rate caused by coupling to molecular vibrations, the energy transport process cannot be resolved by this two-dimensional technique. However, this can be remedied by placing the complex in an optical microcavity. With strong interaction to optical cavities, this two-dimensional technique can capture the exciton-photon hybridization and reveal the relaxation rates as well as energy transfer pathways. The polaritons result in the considerable improvement of the resolution of energy transfer pathways and slow down the energy transfer rate, which could overcome the difficulty caused by the time uncertainty from the spectral gates with the requirement of high frequency resolution for resolving the excited states in LHCII aggregates.[91]

In addition, the relaxation dynamics in some strongly coupled large aggregates and semiconductors illustrated the important role of the typical process so-called exciton-exciton annihilation (EEA),[47–49] which goes beyond the scope of this article. The EEA processes may dominate in short-time exciton dynamics[92] so that it could take place in the comparable time scale as the energy transport rates. The EEA may also be probed by this 2D photon-coincidence counting spectroscopy. The EEA processes would leave a fingerprint when detecting the coincidence-counting signal of photons emitted by the aggregates, in that it could lead to a different scenario of exciton transport.

ACKNOWLEDGMENTS

S.M. and Z.Z. gratefully acknowledge the support of NSF Grant No. CHE-1663822. K.D. is supported by the Zijiang Endowed Young Scholar Fund.

APPENDIX: LIOUVILLIAN IN QUANTUM MASTER EQUATION AND EXPRESSIONS OF SIGNAL

Here $L = L_0 + A$, where $L_0 = -\frac{i}{\hbar}[H_S, *]$ and A originates from the dissipation induced by phonon bath. The matrix elements of Liouvillian L are under secular approximation

$$\begin{aligned}
L_{e_le_l,e_pe_p} &= A_{e_le_l,e_pe_p},\\
L_{f_lf_l,f_pf_p} &= A_{f_lf_l,f_pf_p},\\
L_{e_le_p,e_le_p} &= i(\omega_p^e - \omega_l^e) + A_{e_le_p,e_le_p},\ l \neq p,\\
L_{f_nf_m,f_nf_m} &= i(\omega_m^f - \omega_n^f) + A_{f_nf_m,f_nf_m},\ n \neq m,\\
L_{ge_p,ge_p} &= i\omega_p^e + A_{ge_p,ge_p},\\
L_{e_lf_p,e_lf_p} &= i(\omega_p^f - \omega_l^e) + A_{e_lf_p,e_lf_p},\\
L_{e_pe_l,e_pe_l} &= L^*_{e_le_p,e_le_p},\ l \neq p,\\
L_{f_mf_n,f_mf_n} &= L^*_{f_nf_m,f_nf_m},\ n \neq m,\\
L_{e_pge_pg} &= L^*_{ge_p,ge_p},\\
L_{f_pe_lf_pe_l} &= L^*_{e_lf_p,e_lf_p}
\end{aligned} \tag{A1}$$

and

$$\begin{aligned}
A_{f_lf_l,f_pf_p} &= 2\sum_{m=1}^{N}\Big[G^{m,f}_{lp}G^{m,f}_{pl}\gamma_m(\omega_l^f - \omega_p^f)\\
&\quad - \delta_{lp}\sum_{v=1}^{D_f}G^{m,f}_{vl}G^{m,f}_{lv}\gamma_m(\omega_v^f - \omega_l^f)\Big],\\
A_{e_le_l,e_pe_p} &= 2\sum_{m=1}^{N}\Big[G^{m,e}_{lp}G^{m,e}_{pl}\gamma_m(\omega_l^e - \omega_p^e)\\
&\quad - \delta_{lp}\sum_{v=1}^{D_e}G^{m,e}_{vl}G^{m,e}_{lv}\gamma_m(\omega_v^e - \omega_l^e)\Big].
\end{aligned} \tag{A2}$$

For coherence

$$
\begin{aligned}
A_{f_l f_p, f_l f_p} &= \sum_{m=1}^{N}\left\{2G_{ll}^{m,f}G_{pp}^{m,f}\gamma_m(0) - \sum_{v=1}^{D_f}\left[G_{vl}^{m,f}G_{lv}^{m,f}\gamma_m(\omega_v^f-\omega_l^f) + G_{vp}^{m,f}G_{pv}^{m,f}\gamma_m(\omega_v^f-\omega_p^f)\right]\right\},\ l\neq p,\\
A_{e_l e_p, e_l e_p} &= \sum_{m=1}^{N}\left\{2G_{ll}^{m,e}G_{pp}^{m,e}\gamma_m(0) - \sum_{v=1}^{D_e}\left[G_{vl}^{m,e}G_{lv}^{m,e}\gamma_m(\omega_v^e-\omega_l^e) + G_{vp}^{m,e}G_{pv}^{m,e}\gamma_m(\omega_v^e-\omega_p^e)\right]\right\},\ l\neq p,\\
A_{e_l f_p, e_l f_p} &= \sum_{m=1}^{N}\left[2G_{ll}^{m,e}G_{pp}^{m,f}\gamma_m(0) - \sum_{v=1}^{D_e}G_{vl}^{m,e}G_{lv}^{m,e}\gamma_m(\omega_v^e-\omega_l^e) - \sum_{v=1}^{D_f}G_{vp}^{m,f}G_{pv}^{m,f}\gamma_m(\omega_v^f-\omega_p^f)\right],\\
A_{g e_p, g e_p} &= -\sum_{m=1}^{N}\sum_{v=1}^{D_e}G_{vp}^{m,e}G_{pv}^{m,e}\gamma_m(\omega_v^e-\omega_p^e),
\end{aligned}
\tag{A3}
$$

where $\omega_n^a, (a=e,f)$ is the eigenenergy in e- or f-mainfold, determined by Eq. (5).

The Lorentzian gates in Eq. (19) give rise to the following time-domain detector spectrogram:

$$
D(t,\omega;t',\tau) = \frac{1}{2\sigma_\omega}\theta(t'-t)\theta(t'+\tau-t)e^{-(i\omega+\sigma_T)\tau-2\sigma_T(t'-t)}\left[\theta(\tau)e^{-\sigma_\omega\tau}+\theta(-\tau)e^{\sigma_\omega\tau}\right], \tag{A4}
$$

where σ_T and σ_ω control the resolution in time and frequency domains. Substituting Eq. (A4) into Eq. (18) and truncating up to the 4th order over matter-photon interaction, one obtains the forms of $S_i^{(n)}$, $S_{ii}^{(n)}$ in Eq. (20)

$$
\begin{aligned}
S_i^{(1)} \propto{}& \frac{1}{4\sigma_{\omega_1}\sigma_{\omega_2}}\sum_{n=1}^{D_f}\sum_{p,q=1}^{D_e}\sum_{l=1}^{D_f}\sum_{a=1}^{D_f}\sum_{b=1}^{D_e}\frac{\mu_{e_q f_l}^2\mu_{g e_p}^2 S_{e_p e_p,e_b e_b}S^{-1}_{e_b e_b,e_q e_q}S_{f_l f_l,f_a f_a}S^{-1}_{f_a f_a,f_n f_n}|C_n^{(f)}|^2}{(i\omega_1+\sigma_{T_1}+\sigma_{\omega_1}-L_{g e_p,g e_p})(i\omega_2+\sigma_{T_2}+\sigma_{\omega_2}+\nu_{e_b e_b}-L_{e_q f_l,e_q f_l})}\\
&\times\left\{\frac{1}{i\omega_2-\sigma_{T_2}+\sigma_{\omega_2}+\nu_{f_a f_a}-L_{e_q f_l,e_q f_l}}\left(\frac{e^{-(i\omega_2+\sigma_{T_2}+\sigma_{\omega_2}-L_{e_q f_l,e_q f_l})(t_1-t_2)}e^{\nu_{f_a f_a}t_2}}{i\omega_2+2\sigma_{T_1}+\sigma_{T_2}+\sigma_{\omega_2}-L_{e_q f_l,e_q f_l}}-\frac{e^{-2\sigma_{T_2}(t_1-t_2)}e^{\nu_{f_a f_a}t_1}}{2(\sigma_{T_1}+\sigma_{T_2})-\nu_{f_a f_a}}\right)\right.\\
&\left.+\frac{1}{2\sigma_{T_2}+\nu_{e_b e_b}-\nu_{f_a f_a}}\left(\frac{e^{\nu_{e_b e_b}(t_1-t_2)}e^{\nu_{f_a f_a}t_2}}{2\sigma_{T_1}-\nu_{e_b e_b}}-\frac{e^{-2\sigma_{T_2}(t_1-t_2)}e^{\nu_{f_a f_a}t_1}}{2(\sigma_{T_1}+\sigma_{T_2})-\nu_{f_a f_a}}\right)\right\},
\end{aligned}
\tag{A5}
$$

$$
\begin{aligned}
S_i^{(2)} \propto{}& \frac{1}{4\sigma_{\omega_1}\sigma_{\omega_2}}\sum_{\substack{n,m=1\\(n\neq m)}}^{D_f}\sum_{p,q=1}^{D_e}\sum_{b=1}^{D_e}\frac{\mu_{e_q f_n}\mu_{e_q f_m}\mu_{g e_p}^2 S_{e_p e_p,e_b e_b}S^{-1}_{e_b e_b,e_q e_q}C_n^{(f),*}C_m^{(f)}}{(i\omega_1+\sigma_{T_1}+\sigma_{\omega_1}-L_{g e_p,g e_p})(i\omega_2+\sigma_{T_2}+\sigma_{\omega_2}+\nu_{e_b e_b}-L_{e_q f_m,e_q f_m})}\\
&\times\left\{\frac{1}{i\omega_2-\sigma_{T_2}+\sigma_{\omega_2}+L_{f_n f_m,f_n f_m}-L_{e_q f_m,e_q f_m}}\left(\frac{e^{-(i\omega_2+\sigma_{T_2}+\sigma_{\omega_2}-L_{e_q f_m,e_q f_m})(t_1-t_2)}e^{L_{f_n f_m,f_n f_m}t_2}}{i\omega_2+2\sigma_{T_1}+\sigma_{T_2}+\sigma_{\omega_2}-L_{e_q f_m,e_q f_m}}-\frac{e^{-2\sigma_{T_2}(t_1-t_2)}e^{L_{f_n f_m,f_n f_m}t_1}}{2(\sigma_{T_1}+\sigma_{T_2})-L_{f_n f_m,f_n f_m}}\right)\right.\\
&\left.+\frac{1}{2\sigma_{T_2}+\nu_{e_b e_b}-L_{f_n f_m,f_n f_m}}\left(\frac{e^{\nu_{e_b e_b}(t_1-t_2)}e^{L_{f_n f_m,f_n f_m}t_2}}{2\sigma_{T_1}-\nu_{e_b e_b}}-\frac{e^{-2\sigma_{T_2}(t_1-t_2)}e^{L_{f_n f_m,f_n f_m}t_2}}{2(\sigma_{T_1}+\sigma_{T_2})-L_{f_n f_m,f_n f_m}}\right)\right\},
\end{aligned}
\tag{A6}
$$

$$
\begin{aligned}
S_i^{(3)} \propto{}& \frac{1}{4\sigma_{\omega_1}\sigma_{\omega_2}}\sum_{\substack{n,m=1\\(n\neq m)}}^{D_f}\sum_{\substack{p,q=1\\(p\neq q)}}^{D_e}\frac{\mu_{e_q f_n}\mu_{e_p f_m}\mu_{g e_p}\mu_{g e_q}C_n^{(f),*}C_m^{(f)}}{(i\omega_1+\sigma_{T_1}+\sigma_{\omega_1}-L_{g e_p,g e_p})(i\omega_2+\sigma_{T_2}+\sigma_{\omega_2}+L_{e_q e_p,e_q e_p}-L_{e_q f_m,e_q f_m})}\\
&\times\left\{\frac{1}{i\omega_2-\sigma_{T_2}+\sigma_{\omega_2}+L_{f_n f_m,f_n f_m}-L_{e_q f_m,e_q f_m}}\left(\frac{e^{-(i\omega_2+\sigma_{T_2}+\sigma_{\omega_2}-L_{e_q f_m,e_q f_m})(t_1-t_2)}e^{L_{f_n f_m,f_n f_m}t_2}}{i\omega_2+2\sigma_{T_1}+\sigma_{T_2}+\sigma_{\omega_2}-L_{e_q f_m,e_q f_m}}-\frac{e^{-2\sigma_{T_2}(t_1-t_2)}e^{L_{f_n f_m,f_n f_m}t_1}}{2(\sigma_{T_1}+\sigma_{T_2})-L_{f_n f_m,f_n f_m}}\right)\right.\\
&\left.+\frac{1}{2\sigma_{T_2}+L_{e_q e_p,e_q e_p}-L_{f_n f_m,f_n f_m}}\left(\frac{e^{L_{e_q e_p,e_q e_p}(t_1-t_2)}e^{L_{f_n f_m,f_n f_m}t_2}}{2\sigma_{T_1}-L_{e_q e_p,e_q e_p}}-\frac{e^{-2\sigma_{T_2}(t_1-t_2)}e^{L_{f_n f_m,f_n f_m}t_2}}{2(\sigma_{T_1}+\sigma_{T_2})-L_{f_n f_m,f_n f_m}}\right)\right\}
\end{aligned}
\tag{A7}
$$

and

$$
\begin{aligned}
S_{ii}^{(1)} \propto{}& -\frac{1}{4\sigma_{\omega_1}\sigma_{\omega_2}}\sum_{n=1}^{D_f}\sum_{p,q=1}^{D_e}\sum_{l=1}^{D_f}\sum_{a=1}^{D_f}\sum_{b=1}^{D_e}\frac{\mu_{g e_p}^2\mu_{e_q f_l}^2 S_{e_p e_p,e_b e_b}S^{-1}_{e_b e_b,e_q e_q}S_{f_l f_l,f_a f_a}S^{-1}_{f_a f_a,f_n f_n}|C_n^{(f)}|^2}{(i\omega_1+\sigma_{T_1}+\sigma_{\omega_1}-L_{g e_p,g e_p})(i\omega_2+\sigma_{T_2}-\sigma_{\omega_2}-\nu_{f_a f_a}+L_{f_l e_q,f_l e_q})}\\
&\times\left\{\frac{1}{i\omega_2-\sigma_{T_2}-\sigma_{\omega_2}-\nu_{e_b e_b}+L_{f_l e_q,f_l e_q}}\left(\frac{e^{(i\omega_2-\sigma_{T_2}-\sigma_{\omega_2}+L_{f_l e_q,f_l e_q})(t_1-t_2)}e^{\nu_{f_a f_a}t_2}}{i\omega_2-2\sigma_{T_1}-\sigma_{T_2}-\sigma_{\omega_2}+L_{f_l e_q,f_l e_q}}+\frac{e^{\nu_{e_b e_b}(t_1-t_2)}e^{\nu_{f_a f_a}t_2}}{2\sigma_{T_1}-\nu_{e_b e_b}}\right)\right.\\
&\left.+\frac{1}{2\sigma_{T_2}+\nu_{e_b e_b}-\nu_{f_a f_a}}\left(\frac{e^{\nu_{e_b e_b}(t_1-t_2)}e^{\nu_{f_a f_a}t_2}}{2\sigma_{T_1}-\nu_{e_b e_b}}-\frac{e^{-2\sigma_{T_2}(t_1-t_2)}e^{\nu_{f_a f_a}t_1}}{2(\sigma_{T_1}+\sigma_{T_2})-\nu_{f_a f_a}}\right)\right\},
\end{aligned}
\tag{A8}
$$

$$S_{ii}^{(2)} \propto -\frac{1}{4\sigma_{\omega_1}\sigma_{\omega_2}} \sum_{\substack{n,m=1\\(n\neq m)}}^{D_f} \sum_{p,q=1}^{D_e} \sum_{b=1}^{D_e} \frac{\mu_{e_q f_m}\mu_{e_q f_n}\mu_{g e_p}^2 S_{e_p e_p, e_b e_b} S^{-1}_{e_b e_b, e_q e_q} C_n^{(f),*} C_m^{(f)}}{(i\omega_1 + \sigma_{T_1} + \sigma_{\omega_1} - L_{g e_p, g e_p})(i\omega_2 + \sigma_{T_2} - \sigma_{\omega_2} - L_{f_n f_m, f_n f_m} + L_{f_n e_q, f_n e_q})}$$
$$\times \left\{ \frac{1}{i\omega_2 - \sigma_{T_2} - \sigma_{\omega_2} - \nu_{e_b e_b} + L_{f_n e_q, f_n e_q}} \left(\frac{e^{(i\omega_2 - \sigma_{T_2} - \sigma_{\omega_2} + L_{f_n e_q, f_n e_q})(t_1 - t_2)} e^{L_{f_n f_m, f_n f_m} t_2}}{i\omega_2 - 2\sigma_{T_1} - \sigma_{T_2} - \sigma_{\omega_2} + L_{f_n e_q, f_n e_q}} + \frac{e^{\nu_{e_b e_b}(t_1 - t_2)} e^{L_{f_n f_m, f_n f_m} t_2}}{2\sigma_{T_1} - \nu_{e_b e_b}} \right) \right.$$
$$\left. + \frac{1}{2\sigma_{T_2} + \nu_{e_b e_b} - L_{f_n f_m, f_n f_m}} \left(\frac{e^{\nu_{e_b e_b}(t_1 - t_2)} e^{L_{f_n f_m, f_n f_m} t_2}}{2\sigma_{T_1} - \nu_{e_b e_b}} - \frac{e^{-2\sigma_{T_2}(t_1 - t_2)} e^{L_{f_n f_m, f_n f_m} t_1}}{2(\sigma_{T_1} + \sigma_{T_2}) - L_{f_n f_m, f_n f_m}} \right) \right\}, \tag{A9}$$

$$S_{ii}^{(3)} \propto -\frac{1}{4\sigma_{\omega_1}\sigma_{\omega_2}} \sum_{\substack{n,m=1\\(n\neq m)}}^{D_f} \sum_{\substack{p,q=1\\(p\neq q)}}^{D_e} \frac{\mu_{e_p f_m}\mu_{e_q f_n}\mu_{g e_q}\mu_{g e_p} C_n^{(f),*} C_m^{(f)}}{(i\omega_1 + \sigma_{T_1} + \sigma_{\omega_1} - L_{g e_p, g e_p})(i\omega_2 + \sigma_{T_2} - \sigma_{\omega_2} - L_{f_n f_m, f_n f_m} + L_{f_n e_p, f_n e_p})}$$
$$\times \left\{ \frac{1}{i\omega_2 - \sigma_{T_2} - \sigma_{\omega_2} - L_{e_q e_p, e_q e_p} + L_{f_n e_p, f_n e_p}} \left(\frac{e^{(i\omega_2 - \sigma_{T_2} - \sigma_{\omega_2} + L_{f_n e_p, f_n e_p})(t_1 - t_2)} e^{L_{f_n f_m, f_n f_m} t_2}}{i\omega_2 - 2\sigma_{T_1} - \sigma_{T_2} - \sigma_{\omega_2} + L_{f_n e_p, f_n e_p}} + \frac{e^{L_{e_q e_p, e_q e_p}(t_1 - t_2)} e^{L_{f_n f_m, f_n f_m} t_2}}{2\sigma_{T_1} - L_{e_q e_p, e_q e_p}} \right) \right.$$
$$\left. + \frac{1}{2\sigma_{T_2} + L_{e_q e_p, e_q e_p} - L_{f_n f_m, f_n f_m}} \left(\frac{e^{L_{e_q e_p, e_q e_p}(t_1 - t_2)} e^{L_{f_n f_m, f_n f_m} t_2}}{2\sigma_{T_1} - L_{e_q e_p, e_q e_p}} - \frac{e^{-2\sigma_{T_2}(t_1 - t_2)} e^{L_{f_n f_m, f_n f_m} t_1}}{2(\sigma_{T_1} + \sigma_{T_2}) - L_{f_n f_m, f_n f_m}} \right) \right\}. \tag{A10}$$

S-matrix appeared above is to diagonalize the population block L_{pop} of the Liouvillian L: $S^{-1}L^{(a)}_{\text{pop}}S = \text{diag}\{\nu_{a_i a_i}\}$; $i = 1, 2, \ldots, D_a$; $a \in e, f$. $\nu_{a_i a_i}$'s are the eigenvalues.

[1] S. Nußmann, K. Murr, M. Hijlkema, B. Weber, A. Kuhn, and G. Rempe, Nat. Phys. **1**, 122 (2005).
[2] S. Kena-Cohen and S. R. Forrest, Nat. Photonics **4**, 371 (2010).
[3] J. Bellessa, C. Symonds, J. Laverdant, J. M. Benoit, J. C. Plenet, and S. Vignoli, Electronics **3**, 303 (2014).
[4] A. Cacciola, O. Di Stefano, R. Stassi, R. Saija, and S. Savasta, ACS Nano **8**, 11483 (2014).
[5] Y. Tsuchimoto, H. Nagai, M. Amano, K. Bando, and H. Kondo, Appl. Phys. Lett. **104**, 233307 (2014).
[6] D. M. Coles *et al.*, Nat. Commun. **5**, 5561 (2014).
[7] F. C. Spano, J. Chem. Phys. **142**, 184707 (2015).
[8] F. Herrera and F. C. Spano, Phys. Rev. Lett. **116**, 238301 (2016).
[9] M. Kowalewski, K. Bennett, and S. Mukamel, J. Chem. Phys. **144**, 054309 (2016).
[10] Z. D. Zhang and J. Wang, J. Chem. Phys. **140**, 245101 (2014).
[11] M. Kowalewski, K. Bennett, and S. Mukamel, J. Phys. Chem. Lett. **7**, 2050 (2016).
[12] J. Bellessa, C. Bonnand, J. C. Plenet, and J. Mugnier, Phys. Rev. Lett. **93**, 036404 (2004).
[13] A. Shalabney, J. George, J. Hutchison, G. Pupillo, C. Genet, and T. W. Ebbesen, Nat. Commun. **6**, 5981 (2015).
[14] T. W. Ebbesen, Acc. Chem. Res. **49**, 2403 (2016).
[15] A. Thomas *et al.*, Angew. Chem., Int. Ed. **55**, 11462 (2016).
[16] O. Kühn, V. Chernyak, and S. Mukamel, J. Chem. Phys. **105**, 8586 (1996).
[17] O. Kühn and S. Mukamel, J. Phys. Chem. B **101**, 809 (1997).
[18] D. M. Coles, N. Somaschi, P. Michetti, C. Clark, P. G. Lagoudakis, P. G. Savvidis, and D. G. Lidzey, Nat. Mater. **13**, 712 (2014).
[19] A. D. Dunkelberger, B. T. Spann, K. P. Fears, B. S. Simpkins, and J. C. Owrutsky, Nat. Commun. **7**, 13504 (2016).
[20] F. Caruso *et al.*, Phys. Rev. B **85**, 125424 (2012).
[21] V. Novoderezhkin, M. A. Palacios, H. van Amerongen, and R. van Grondelle, J. Phys. Chem. B **108**, 10363 (2004).
[22] V. Novoderezhkin, J. M. Salverda, H. van Amerongen, and R. van Grondelle, J. Phys. Chem. B **107**, 1893 (2003).
[23] V. I. Novoderezhkin, M. A. Palacios, H. van Amerongen, and R. van Grondelle, J. Phys. Chem. B **109**, 10493 (2005).
[24] V. I. Novoderezhkin, A. Marin, and R. van Grondelle, Phys. Chem. Chem. Phys. **13**, 17093 (2011).
[25] M. M. Enriquez, P. Akhtar, C. Zhang, G. Garab, P. H. Lambrev, and H. S. Tan, J. Chem. Phys. **142**, 212432 (2015).
[26] F. Muäh, M. E. A. Madjet, and T. Renger, J. Phys. Chem. B **114**, 13517 (2010).
[27] D. Abramavicius, B. Palmieri, D. V. Voronine, F. Sanda, and S. Mukamel, Chem. Rev. **109**, 2350 (2009).
[28] S. Mukamel and R. F. Loring, J. Opt. Soc. Am. B **3**, 595 (1986).
[29] L. E. Fried and S. Mukamel, Adv. Chem. Phys. **84**, 435 (1993).
[30] R. Berera *et al.*, Proc. Natl. Acad. Sci. U. S. A. **103**, 5343 (2006).
[31] S. Mukamel and Y. Tanimura, J. Chem. Phys. **99**, 9496 (1993).
[32] D. A. Blank, L. J. Kaufman, and G. R. Fleming, J. Chem. Phys. **111**, 3105 (1999).
[33] G. D. Scholes, G. R. Fleming, A. Olaya-Castro, and R. van Grondelle, Nat. Chem. **3**, 763 (2011).
[34] H. Lee, Y.-C. Cheng, and G. R. Fleming, Science **316**, 1462 (2007).
[35] A. Ishizaki and G. R. Fleming, Annu. Rev. Condens. Matter Phys. **3**, 333 (2012).
[36] G. S. Engel *et al.*, Nature **446**, 782 (2007).
[37] E. Collini *et al.*, Nature **463**, 644 (2010).
[38] Z. D. Zhang and J. Wang, Sci. Rep. **6**, 37629 (2016).
[39] Z. D. Zhang and J. Wang, J. Phys. Chem. B **119**(13), 4662 (2015).
[40] R. van Grondelle and V. I. Novoderezhkin, Phys. Chem. Chem. Phys. **8**, 793 (2006).
[41] G. Panitchayangkoon *et al.*, Proc. Natl. Acad. Sci. U. S. A. **107**, 12766 (2010).
[42] I. Kassal and A. Aspuru-Guzik, New J. Phys. **14**, 053041 (2012).
[43] A. W. Chin, A. Datta, F. Caruso, S. F. Huelga, and M. B. Plenio, New J. Phys. **12**, 065002 (2010).
[44] Z. D. Zhang, H. C. Fu, and J. Wang, Phys. Rev. B **95**, 144306 (2017).
[45] J. Chmeliov, W. P. Bricker, C. Lo, E. Jouin, L. Valkunas, A. V. Ruban, and C. D. P. Duffy, Phys. Chem. Chem. Phys. **17**, 15857 (2015).
[46] G. S. Schlau-Cohen, H.-Y. Yang, T. P. J. Krger, P. Xu, M. Gwizdala, R. van Grondelle, R. Croce, and W. E. Moerner, J. Phys. Chem. Lett. **6**, 860 (2015).
[47] C. D. P. Duffy, J. Chmeliov, M. Macernis, J. Sulskus, L. Valkunas, and A. V. Ruban, J. Phys. Chem. B **117**, 10974 (2013).
[48] J. Standfuss, A. C. T. van Scheltinga, M. Lamborghini, and W. Kühlbrandt, EMBO J. **24**, 919 (2005).
[49] L. Valkunas, I. H. M. van Stokkum, R. Berera, and R. van Grondelle, Chem. Phys. **357**, 17 (2009).
[50] W. Kühlbrandt, D. N. Wang, and Y. Fujiyoshi, Nature **367**, 614 (1994).
[51] H. van Amerongen and R. van Grondelle, J. Phys. Chem. B **105**, 604 (2001).
[52] A. Ishizaki and G. R. Fleming, J. Chem. Phys. **130**, 234111 (2009).
[53] A. Ishizaki and G. R. Fleming, New J. Phys. **12**, 055004 (2010).
[54] G. Panitchayangkoona, D. V. Voronine, D. Abramavicius, J. R. Caram, N. H. C. Lewis, S. Mukamele, and G. S. Engel, Proc. Natl. Acad. Sci. U. S. A. **108**, 20908 (2011).
[55] M. Sarovar, A. Ishizaki, G. R. Fleming, and K. B. Whaley, Nat. Phys. **6**, 462 (2010).
[56] M. Mohseni, P. Rebentrost, S. Lloyd, and A. Aspuru-Guzik, J. Chem. Phys. **129**, 174106 (2008).

[57]K. E. Dorfman, D. V. Voronine, S. Mukamel, and M. O. Scully, Proc. Natl. Acad. Sci. U. S. A. **110**, 2746 (2013).
[58]E. Romero, R. Augulis, V. I. Novoderezhkin, M. Ferretti, J. Thieme, D. Zigmantas, and R. van Grondelle, Nat. Phys. **10**, 676 (2014).
[59]J. Yuen-Zhou, D. Arias, D. Eisele, J. J. Krich, C. Steiner, K. A. Nelson, and A. Aspuru-Guzik, ACS Nano **8**, 5527 (2014).
[60]T. R. Calhoun, N. S. Ginsberg, G. S. Schlau-Cohen, Y.-C. Cheng, M. Ballottari, R. Bassi, and G. R. Fleming, J. Phys. Chem. B **113**, 16291 (2009).
[61]G. S. Schlau-Cohen, A. Ishizaki, T. R. Calhoun, N. S. Ginsberg, M. Ballottari, R. Bassi, and G. R. Fleming, Nat. Chem. **4**, 389 (2012).
[62]G. D. Scholes *et al.*, Nature **543**, 647 (2017).
[63]H. G. Duan, V. I. Prokhorenko, R. J. Cogdell, K. Ashraf, A. L. Stevens, M. Thorwart, and R. J. Dwayne Miller, Proc. Natl. Acad. Sci. U. S. A. **114**, 8493 (2017).
[64]D. M. Wilkins and N. S. Dattani, J. Chem. Theory Comput. **11**, 3411 (2015).
[65]A. Ishizaki, T. R. Calhoun, G. S. Schlau-Cohen, and G. R. Fleming, Phys. Chem. Chem. Phys. **12**, 7319 (2010).
[66]E. Collini and G. D. Scholes, Science **323**, 369 (2009).
[67]Z. G. Yu, M. A. Berding, and H. B. Wang, Phys. Rev. E **78**, 050902(R) (2008).
[68]A. Ishizaki and G. R. Fleming, J. Phys. Chem. B **115**, 6227 (2011).
[69]M. J. Nee, C. R. Baiz, J. M. Anna, R. McCanne, and K. J. Kubarych, J. Chem. Phys. **129**, 084503 (2008).
[70]G. S. Schlau-Cohen, T. R. Calhoun, N. S. Ginsberg, E. L. Read, M. Ballottari, R. Bassi, R. van Grondelle, and G. R. Fleming, J. Phys. Chem. B **113**, 15352 (2009).
[71]H. van Amerongen, L. Valkunas, and R. van Grondelle, *Photosynthetic Excitons* (World Scientific, Singapore, 2000), Chap. 8.
[72]H. Rogl, R. Schodel, H. Lokstein, W. Kuhlbrandt, and A. Schubert, Biochemistry **41**, 2281 (2002).
[73]R. Agarwal, B. P. Krueger, G. D. Scholes, M. Yang, J. Yom, L. Mets, and G. R. Fleming, J. Phys. Chem. B **104**, 2908 (2000).
[74]J. M. Salverda, M. Vengris, B. P. Krueger, G. D. Scholes, A. R. Czamoleski, V. Novoderezhkin, H. van Amerongen, and R. van Grondelle, Biophys. J. **84**, 450 (2003).
[75]W. M. Zhang, T. Meier, V. Chernyak, and S. Mukamel, J. Chem. Phys. **108**, 7763 (1998).
[76]D. Abramavicius, D. V. Voronine, and S. Mukamel, Biophys. J. **94**, 3613 (2008).
[77]D. Abramavicius and S. Mukamel, J. Chem. Phys. **133**, 064510 (2010).
[78]Y. Zhao, T. Meier, W. M. Zhang, V. Chernyak, and S. Mukamel, J. Phys. Chem. B **103**, 3954 (1999).
[79]S. Mukamel, D. Abramavicius, L. Yang, W. Zhuang, I. V. Schweigert, and D. Voronine, Acc. Chem. Res. **42**, 553 (2009).
[80]K. E. Dorfman and S. Mukamel, Phys. Scr. **91**, 083004 (2016).
[81]K. E. Dorfman and S. Mukamel, Phys. Rev. A **86**, 023805 (2012).
[82]K. E. Dorfman and S. Mukamel, Phys. Rev. A **86**, 013810 (2012).
[83]K. E. Dorfman and S. Mukamel, "Multidimensional photon correlation spectroscopy of cavity polaritons," Proc. Natl. Acad. Sci. U. S. A. (published online).
[84]Z. Liu, H. Yan, K. Wang, T. Kuang, J. Zhang, L. Gui, X. An, and W. Chang, Nature **428**, 287 (2004).
[85]M. Becker, V. Nagarajan, and W. W. Parson, J. Am. Chem. Soc. **113**, 6840 (1991).
[86]E. J. G. Peterman, T. Pullerits, R. van Grondelle, and H. J. van Amerongen, J. Phys. Chem. B **101**, 4448 (1997).
[87]J. Pieper, J. Voigt, and G. J. Small, J. Phys. Chem. B **103**, 2319 (1999).
[88]M. O. Scully and M. S. Zubairy, *Quantum Optics* (Cambridge University Press, 1997).
[89]R. H. Dicke, Phys. Rev. **93**, 99 (1954).
[90]N. G. Stoltz, M. Rakher, S. Strauf, A. Badolato, D. D. Lofgreen, P. M. Petroff, L. A. Coldren, and D. Bouwmeester, Appl. Phys. Lett. **87**, 031105 (2005).
[91]A. Aspect, G. Roger, S. Reynaud, J. Dalibard, and C. Cohen-Tannoudji, Phys. Rev. Lett. **45**, 617 (1980).
[92]M. Vengris, D. S. Larsen, L. Valkunas, G. Kodis, C. Herrero, D. Gust, T. Moore, A. Moore, and R. van Grondelle, J. Phys. Chem. B **117**, 11372 (2013).